

communications physics

ARTICLE



<https://doi.org/10.1038/s42005-021-00619-y>

OPEN

Merohedral disorder and impurity impacts on superconductivity of fullerenes

Shu-Ze Wang ^{1,5}, Ming-Qiang Ren^{1,5}, Sha Han¹, Fang-Jun Cheng¹, Xu-Cun Ma^{1,2}, Qi-Kun Xue^{1,2,3,4} & Can-Li Song ^{1,2}

Local quasiparticle states around impurities provide essential insight into the mechanism of unconventional superconductivity, especially when the candidate materials are proximate to an antiferromagnetic Mott-insulating phase. While such states have been reported in atom-based cuprates and iron-based compounds, they are unexplored in organic superconductors which feature tunable molecular orientation. Here we employ scanning tunneling microscopy and spectroscopy to reveal multiple forms of robustness of an exotic s-wave superconductivity in epitaxial Rb₃C₆₀ films against merohedral disorder, non-magnetic single impurities and step edges at the atomic scale. Yu-Shiba-Rusinov (YSR) states, induced by deliberately incurred Fe adatoms that act as magnetic scatterers, have also been observed. The YSR bound states show abrupt spatial decay and vary in energy with the Fe adatom registry. These results and a doping-dependent study of superconductivity point towards local electron pairing in which the multiorbital electronic correlations and intramolecular phonons together drive the high-temperature superconductivity of doped fullerenes.

¹State Key Laboratory of Low-Dimensional Quantum Physics, Department of Physics, Tsinghua University, Beijing, China. ²Frontier Science Center for Quantum Information, Beijing, China. ³Beijing Academy of Quantum Information Sciences, Beijing, China. ⁴Southern University of Science and Technology, Shenzhen, China. ⁵These authors contributed equally: Shu-Ze Wang, Ming-Qiang Ren. email: clsong07@mail.tsinghua.edu.cn

Disorders, impurities in an otherwise homogeneous or granular superconductor, are often undesired aliens because they may hinder observations of intrinsic properties of the host material^{1–4}. Yet, dopant impurities could also be a double-edged sword by leading not only to emergent high-temperature (T_c) superconductivity in cuprates and iron pnictides^{5,6} but also to uncovering the underlying mechanism of unconventional superconductivity^{7–13}, especially as multiple unusual states are complexly intertwined in these materials^{14,15}. Whereas it has been well documented that non-magnetic impurities little affect Cooper pairs in conventional superconductors^{16,17}, they induce local bound states in the superconducting gap (Δ) and suppress superconductivity via pair breaking for unconventional pairing symmetries, for example, in a d -wave or s_{\pm} wave superconductor^{8,17–20}. Recently, anomalous enhancement of superconductivity by disorder is another example of impurities revealing their fundamental significance for low-dimensional superconductors^{21–24}. It is therefore tempting to consider impurities as a blessing in disguise to unveil the physics of candidate superconductors^{4–20}, to strive for optimal superconductivity with T_c and Δ reaching their respective maxima²⁵, and to create exotic electronic states that never emerge from pure superconducting systems²⁶.

Unlike atom-based superconductors, an organic superconductor is a synthetic molecule-based compound that uniquely exhibits additional degrees of freedom related to its molecular orientation. Consequently, inequivalent molecular orientations take place. Such orientational (merohedral) disorder has been seen early in pure and doped fullerenes^{27,28}, but its impact, either harmful^{29,30} or irrelevant^{31,32}, to superconductivity of fullerenes, is highly controversial. In addition, the fullerides represent an unusual category of organic superconductors in which the multiorbital electronic correlations and electron–phonon interactions are both suggested to be significant to reach high- T_c superconductivity^{33,34}. Under this context, a systematic study of impurity effects on superconductivity of doped fullerenes would provide justification of the previously advocated s -wave pairing symmetry^{35–37}, as well as advance the understanding of the superconducting state. However, such an experiment is unexplored and the roles played by magnetic and non-magnetic impurities remain unknown in fulleride superconductors.

In this work, we use a molecular beam epitaxy (MBE) technique to grow epitaxial films of rubidium (Rb)-doped fullerenes with thickness and filling tunability, and probe the local quasiparticle states in the vicinity of various impurities at the atomic scale by means of cryogenic scanning tunneling microscopy (STM) and spectroscopy (STS). Distinct from the superconducting K_3C_{60} films without merohedral disorder³⁷ and the insulating Cs_3C_{60} ones with great merohedral disorder³⁸, merohedrally disordered Rb_3C_{60} films are superconducting. This allows for atomic-scale visualization of merohedral disorder impact on superconductivity of fullerenes, which, together with a detailed STS study of magnetic and non-magnetic impurities, shows that superconductivity of fullerenes is entirely consistent with local s -wave pairing. By studying the thickness and electron-filling dependence of superconducting gap Δ in Rb_xC_{60} , we further establish a unified phase diagram of fullerenes in which the optimal superconductivity always develops at half-filling ($x = 3$).

Results

Merohedral disorder and its impact on superconductivity. Figure 1a depicts a representative STM topography of nine monolayer (ML) Rb_3C_{60} thin films epitaxially grown on graphitized SiC(0001) substrates. Evidently, not all C_{60} molecules have the same orientation, although one threefold symmetry axis for

every C_{60} is perpendicular to the surface. Specifically, nanoscale domains with two distinct C_{60} orientations, related by 44.48° rotation about the [111] axis (Fig. 1b), develop and are partially opacified in red and orange, respectively. This is reminiscent of the two standard orientations of C_{60} that randomly occur and cause merohedral disorder in face-centered cubic-structured trivalent fullerides^{28–30}. The C_{60} orientations are more disordered in regions between adjacent merohedral domains. In order to quantify the merohedral disorder, the averaged orientational correlation functions $\langle \cos(\theta_{ij}) \rangle^{39}$, in which $\theta_{ij} = \theta_i - \theta_j$ denotes the angle between nearest-neighbor C_{60} molecules (i.e., i and j), are calculated and summarized in Fig. 1c. The orientational correlation decreases with alkali metal radius, indicating increasing merohedral disorder. This most probably arises from a weakening of Coulomb repulsion between adjacent trivalent C_{60} ions associated with the lattice expansion⁴⁰, which otherwise stabilizes a long-ranged merohedral order in the K_3C_{60} films³⁷, to wit $\langle \cos(\theta_{ij}) \rangle = 1$. For a specific K_3C_{60} or Rb_3C_{60} compound, it turns out that the orientational correlation and thus merohedral disorder change little with the film thickness (Supplementary Figure 1).

Tunneling spectroscopy of fullerides probes the local density of quasiparticle states (DOS) and measures the superconducting energy gap at the Fermi level (E_F). In Fig. 1d, we compare tunneling dI/dV spectra on various trivalent fulleride films A_3C_{60} ($A = K, Rb, Cs$) with the same thickness of 9 ML. Although two sharp DOS peaks develop ~ 0.4 eV and 0.1 eV in the merohedrally ordered K_3C_{60} films³⁷, they are largely smoothed out in both Rb_3C_{60} and $RbCs_2C_{60}$ with the great merohedral disorder. This observation is consistent with the theoretical calculation that the merohedral disorder would blur t_{1u} -derived DOS peaks in A_3C_{60} ⁴¹. It is, however, worth noting that the low-lying DOS width estimated as the spacing between the two conductance minima below and above E_F (> 1.2 eV, see the two dashed lines in Fig. 1d) is significantly larger than the commonly argued t_{1u} bandwidth of ~ 0.5 eV^{41,42}. Such a discrepancy might originate from the Jahn-Teller (JT) instabilities and Coulomb interactions omitted by three-band first-principles calculations^{41,42}. In consideration of JT-induced subband splitting and electronic correlations, the t_{1u} bandwidth could be substantially increased^{34,43,44} and accords with our observation. A further enhancement of electronic correlations U in the most expanded Cs_3C_{60} films pushes the t_{1u} -derived DOS toward higher energy and opens a Mott-insulating gap³⁸, in contrast to the superconducting ground state in K_3C_{60} and Rb_3C_{60} (Fig. 1d).

Despite nanoscale merohedral disorder, superconductivity develops well in Rb_3C_{60} films. We unambiguously reveal this by measuring the spatial dependence of superconducting gaps at the atomic scale via STS, as exemplified in Fig. 1e. Even on the boundaries between adjacent merohedral domains, the superconducting gaps exhibit clear coherence peaks (blue curves) and are immune to the local merohedral disorder (Fig. 1a). This is further confirmed in Cs and Rb co-doped $RbCs_2C_{60}$ films, which imprint a comparably large merohedral disorder but exhibit a superconducting transition temperature up to $T_c = 23$ K (Supplementary Figure 2). Nevertheless, the superconducting spectra present some spatial electronic inhomogeneities, especially for the coherence peaks. A careful examination of Rb_3C_{60} films at varied thicknesses and spatial locations reveals that the coherence peak amplitude scales inversely with Δ (Supplementary Figure 3). This is unexpected by the conventional wisdom of Bardeen-Cooper-Schrieffer (BCS) picture, and we ascribe to coexistence of competing order, e.g., the ubiquitous pseudogap phase (Supplementary Figure 4)³⁷. Similar behavior and pseudogap phenomenology have been documented in cuprate superconductors⁴⁵.

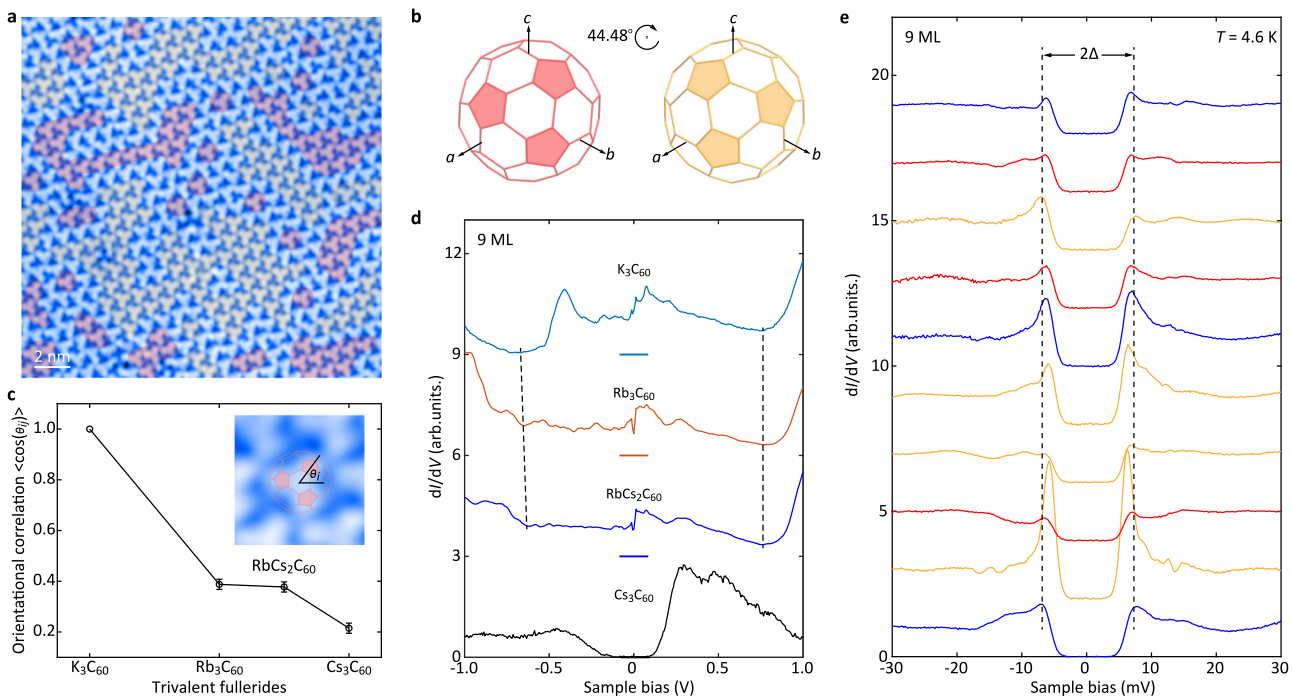


Fig. 1 Merohedral disorder and superconductivity in Rb₃C₆₀. **a**, Scanning tunneling microscopy (STM) topography (20 nm × 20 nm, $V = 1.0$ V, $I = 30$ pA) on nine monolayer (ML) Rb₃C₆₀ films. The V and I represent the applied sample bias and tunneling current, respectively. Two standard orientations of C₆₀ related by 44.48° rotation about the [111] axis are partially opacified in red and orange, respectively. **b**, Schematic view of the two standard orientations of C₆₀ molecules along the [111] direction. **c**, Alkali metal ion dependence of the orientational correlation of C₆₀ molecules (i.e., merohedral disorder). The statistical errors indicate the standard derivations of the merohedral disorder measured in various regions. Inset: definition of the angle θ_i of C₆₀ orientation with respect to the horizontal axis. **d**, Spatially averaged differential conductance dI/dV spectra on 9 ML A₃C₆₀ ($A = K, Rb, Cs$) films. The spectra have been vertically offset for clarity, with their zero conductance positions marked by correspondingly colored horizontal lines. Setpoint: $V = 1.0$ V and $I = 200$ pA. **e**, Conductance dI/dV spectra ($V = 30$ mV and $I = 200$ pA) taken at equal separation (2.8 nm) along the diagonal line from top left to the bottom right and color-coded to match the C₆₀ domains in **a**.

Thickness and filling dependence of superconductivity. Having established the merohedral disorder-independent superconductivity in fullerides, we then explore its dependence on thickness and electron filling. Elaborated in Fig. 2a–c is the temperature dependence of spatially averaged dI/dV spectra measured on 3 ML, 6 ML, and 9 ML Rb₃C₆₀, respectively. Again, the fully gapped superconductivity with an isotropic s-wave pairing is consistently confirmed in Rb₃C₆₀ and gets smeared out at elevated temperatures. By examining the temperature dependence of the gap depth in Fig. 2d, the critical temperature T_c is determined and increases from 23 K for 3 ML, to 26 K for 6 ML, and 28 K for 9 ML Rb₃C₆₀. Such a T_c evolution with film thickness stands in marked contrast to K₃C₆₀, where the maximum T_c occurs in 3 ML films³⁷. This hints at other factor, possibly linking with alkali metal-dependent electronic correlations (U)³⁶, to consider for a unified understanding of superconductivity of A₃C₆₀ films at varied thicknesses. Note that due to the significantly increased U monolayer and bilayer Rb₃C₆₀ films are non-superconducting at all (Supplementary Figure 5), in analogy to the K₃C₆₀ counterparts³⁷. A residual DOS depletion around E_F , hence pseudogap, is also observed in all superconducting Rb₃C₆₀ films above T_c (see the red curves in Fig. 2a–c) and within vortices (Supplementary Figure 4b).

In what follows, we explore the superconductivity of Rb_xC₆₀ by tuning the stoichiometry and thus electron filling x . Figure 2e summarizes the superconducting gap Δ (top panel) and averaged orientational correlation (bottom panel) as a function of Rb doping level x . Clearly, Δ increases with the film thickness, in good accordance with T_c (Fig. 2d). The extracted reduced gap ratio $2\Delta/k_B T_c = 6.0 \pm 0.4$ is comparable to that of K_xC₆₀ films³⁷,

but appreciably exceeds the canonical BCS value of 3.53. Interestingly, Δ reaches its peak at half-filling irrespective of film thickness, and declines more quickly below half-filling for thin Rb₃C₆₀ films. Notwithstanding a dome-shaped variation of Δ , the merohedral disorder remains unchanged with electron filling x and film thickness (bottom panel of Fig. 1e). This not only corroborates the above claim that superconductivity is little influenced by merohedral disorder^{31,46}, but also hints that the dome-shaped superconducting phase diagram does not correlate from any x -dependent merohedral disorder effects.

Robust superconductivity against non-magnetic impurities. As the electron doping of Rb_xC₆₀ deviates slightly from half-filling, subsurface tetragonal Rb vacancies emerge as dark windmills as $x < 3$, whereas excess K adatoms appear and occupy the octahedral sites as $x > 3$. Analogous to K_xC₆₀ (Supplementary Figure 6a, b)³⁷, they do not alter profoundly the orientation of nearby fullerene molecules and thus serve as intrinsically non-magnetic impurities to test the fully gapped superconductivity in fullerides. Figure 3a–d shows the STM topographies of a single Rb vacancy and an excess Rb adatom, as well as linecut dI/dV spectra taken across both impurities. No in-gap bound state is revealed (red curves), although Δ shrinks by ~25% on Rb excess impurity (Supplementary Figure 7a, b). Similar responses of the superconducting gap to K impurities have been observed in K_xC₆₀ as well (Supplementary Figure 6c). Here the Δ reduction possibly arises from a local doping variation, namely a deviation of x from 3. The vacancies are located beneath the top C₆₀ molecules, rendering the local Δ reduction invisible for surface-sensitive STS.

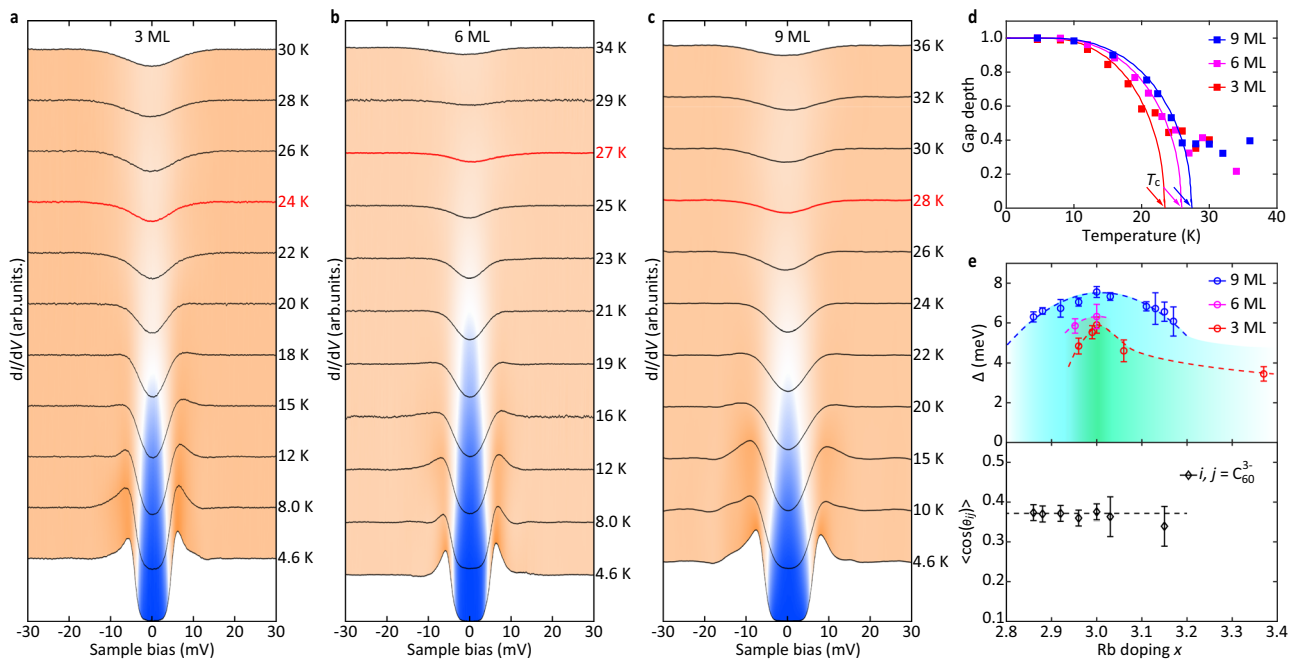


Fig. 2 Thickness dependence of superconductivity. **a–c** Spatially averaged and normalized conductance dI/dV spectra as a function of temperature and thickness of Rb_3C_{60} films as indicated. The normalization was performed by dividing the raw tunneling spectrum by its background, which was extracted from a cubic fit the conductance for $|V| > 10$ mV. Setpoint: $V = 30$ mV and $I = 200$ pA. The red curves denote the residual pseudogap justly above the superconducting transition temperature (T_c). **d** Dependence of the superconducting gap depth on temperature, yielding a gradual increase of T_c with film thickness (see the guided solid lines and arrows). Here the gap depth denotes the difference between unity and the normalized zero-energy conductance. **e** Electronic phase diagram showing the evolution of superconducting energy gap Δ (empty circles) and averaged orientational correlation (diamonds) as a function of Rb doping x . Note that the orientational correlation function $\langle \cos(\theta_{ij}) \rangle$ is only averaged over the trivalent C_{60} molecules to minimize any disruption by Rb impurities and excess atoms away from half-filling.

On the other hand, step edges could be seen as one-dimensional perturbations and bring about Andreev bound states as they are normal to the possible sign-changing direction in Δ ^{45,47}. The spectroscopic signature of these bound states, e.g., a zero-bias conductance peak (ZBCP), has been observed experimentally in a few cuprate and iron-pnictide superconductors^{45,48,49}. Figure 3e depicts a topographic STM image of one monomolecular step edge separating Rb_3C_{60} epitaxial films between 8 ML (lower terrace) and 9 ML (upper terrace). Note that all step edges run along the close-packed directions of C_{60} molecules. Figure 3f shows dI/dV spectra taken along a trajectory approaching the step edge (solid line in Fig. 3e). The superconducting gap remains undisturbed at the step edge and nearby, and no evidence of Andreev bound states is found (Supplementary Figure 7c). Some random variations in the coherence peak, including strong coherence peaks near Rb excess impurity in Fig. 3d, might be related to the slight electronic inhomogeneity of superconducting Rb_3C_{60} films (Fig. 1e).

Local probe of Yu-Shiba-Rusinov states. To fully understand the impurity impact on fulleride superconductivity, we intentionally deposited Fe atoms on Rb_3C_{60} surface at low temperature (~ 100 K). Single Fe adatoms formed (bright protrusions) and occupied top or hollow sites of the surface C_{60} lattice, dubbed as Fe(I) and Fe(II) in Fig. 4a. Figure 4b represents the dI/dV spectra on both Fe impurities and defect-free regions. Note that multiple Fe(I) and Fe(II) impurities have been measured and averaged to eliminate the spatial inhomogeneity effects on dI/dV spectra. Evidently, both Fe(I) and Fe(II) adatoms act as magnetic scatterers and significantly suppress the superconducting coherence peaks, whereas a prominent ZBCP is clearly observed on Fe(I). They are hallmarks of the Yu-Shiba-Rusinov (YSR) states induced by coupling of

magnetic impurity to an s -wave superconductor^{10,12,16,17,26,50–53}. Figure 4c shows a series of tunneling spectra across an isolated Fe (I) impurity. The ZBCP intensity decreases quite abruptly and gets barely visible at a spatial distance of 1.4 nm from the impurity site. Here the distinct behaviors of YSR states on Fe(I) and Fe(II) may be caused by the varied coupling strength between them and the Rb_3C_{60} films⁵⁴. In other words, the exchange coupling of Fe(II) adsorbed at the hollow sites to Copper pairs might be so significantly weak that the YSR states nearly merge into the superconducting gap edges and are little discernible. Further theoretical analysis is needed to comprehensively understand the Fe registry site-dependent YSR bound states in fulleride superconductors.

Discussion

Our atomic-scale observations of short-range YSR bound states on magnetic Fe adatoms, robust superconductivity against non-magnetic merohedral disorder and impurities compellingly confirm a sign-unchanged s -wave pairing state in fulleride superconductors¹⁷. Distinct from a conventional superconductor, however, in charged fullerenes the t_{1u} -derived conduction band of ~ 0.5 eV is narrow and comparable to the electron-vibron interactions, thereby causing a breakdown of the Migdal's theorem^{55–57}. As a result, superconductivity with local nonretarded attractive interactions^{33,34} is less sensitive to the distribution of the electronic DOS in conduction band⁵⁸, and instead determined by some ensemble-averaged DOS⁵⁹. This differs from the classic BCS superconductors where T_c is essentially governed by the DOS at E_F , and happens to match our finding, i.e., the merohedral disorder considerably modifies the t_{1u} -derived DOS distribution but never affect superconductivity (Fig. 1d, e). Such local electron pairing^{33,34}, mediated by intramolecular JT phonons^{60,61}, has also been reinforced by a short coherence length in fullerides. As estimated from

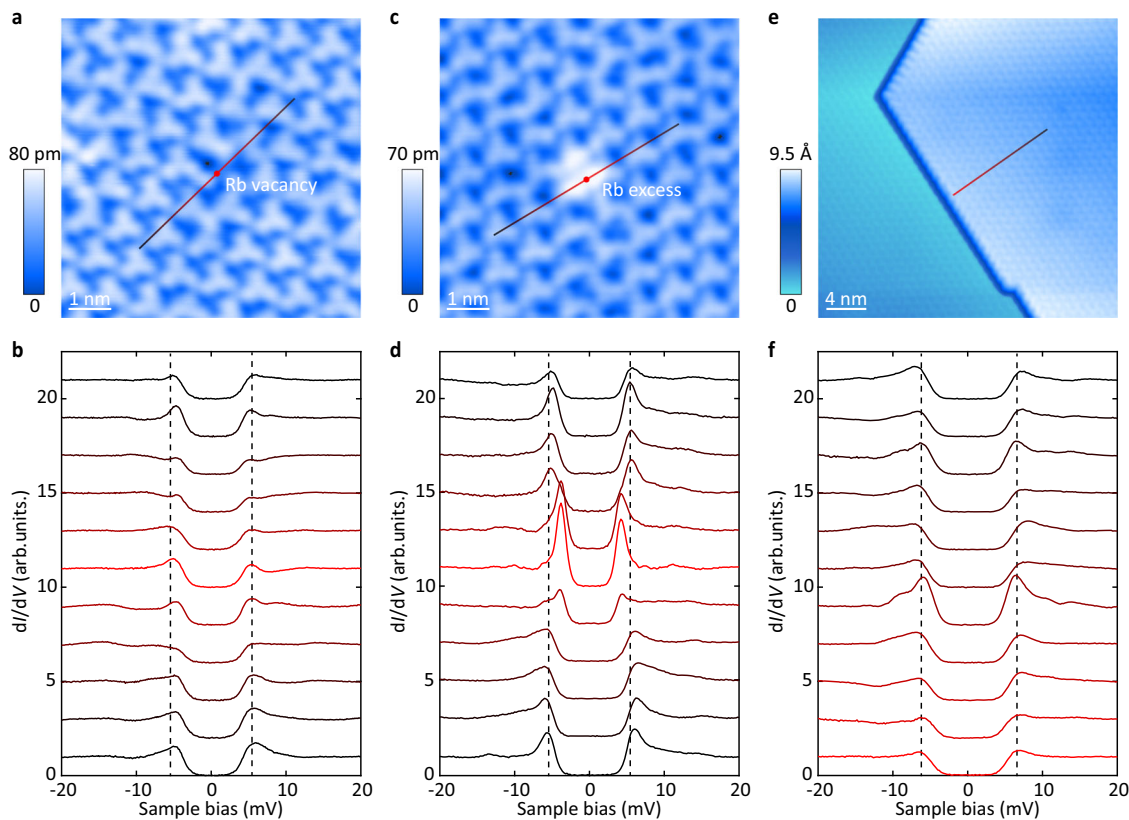


Fig. 3 Immunity of fulleride superconductivity to non-magnetic impurities. **a, b** High-resolution STM topography ($7 \text{ nm} \times 7 \text{ nm}$, $V = 1.0 \text{ V}$, $I = 20 \text{ pA}$) of a single Rb vacancy (red dot) and tunneling spectra acquired 0.5 nm apart along the colored line in **a**. **c, d** STM topography ($7 \text{ nm} \times 7 \text{ nm}$, $V = 1.0 \text{ V}$, $I = 20 \text{ pA}$) of a single Rb excess impurity (red dot) and tunneling spectra acquired 0.5 nm apart along the colored line in **c**. **e, f** STM topography ($30 \text{ nm} \times 30 \text{ nm}$, $V = 1.0 \text{ V}$, $I = 20 \text{ pA}$) of Rb_3C_{60} films with a monomolecular step edge and tunneling spectra acquired 1.3 nm apart along the colored line in **e**. The tunneling spectra are color-coded to match the probed positions near (red) and away from impurities (black). The tunneling gap is set at $V = 30 \text{ mV}$ and $I = 200 \text{ pA}$. Note that two different color gradients are used in **a, c**, and **e**.

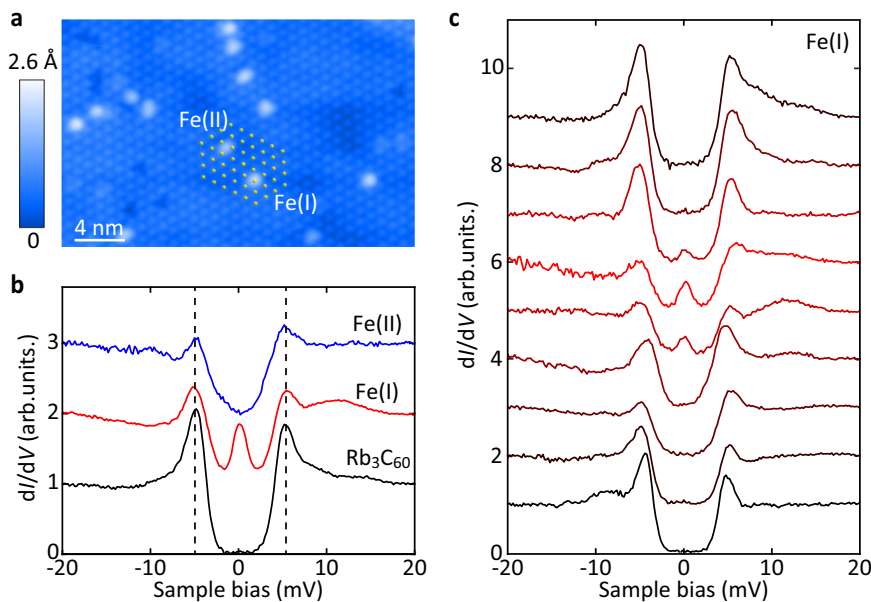


Fig. 4 Magnetic impurity (Fe)-induced bound states. **a** STM topography ($28 \text{ nm} \times 18 \text{ nm}$, $V = 2.0 \text{ V}$, $I = 30 \text{ pA}$) of superconducting Rb_3C_{60} films upon intentional post-deposition of tiny Fe adatoms. The yellow dots indicate the topmost C_{60} molecules. **b** Comparison of tunneling conductance dI/dV spectra averaged over single Fe(I), Fe(II) impurities, and locations far from any impurities. Black vertical dashes denote the energy positions of the superconducting gap. **c** Linecut dI/dV spectra taken at equal separations (0.7 nm) across an isolated Fe(I) impurity. The red curve is measured just on the impurity site. Setpoint: $V = 30 \text{ mV}$ and $I = 200 \text{ pA}$.

the vortex core radius (Supplementary Figure 4a,c), the coherence length of a Cooper pair is 1.5 ± 0.2 nm in Rb_3C_{60} and 2.6 ± 0.5 nm in K_3C_{60} ³⁷, respectively, which are only about twice the separation between nearest-neighbor fullerene molecules.

In the local pairing mechanism, the key ingredients for high- T_c superconductivity are the strong coupling of the t_{1u} electrons to intramolecular JT phonons in trivalent fullerides^{59–61}. The phonon-mediated unusual multiorbital (attractive) interactions lead to an effectively inverted Hund's coupling ($S = 1/2$)³⁶ and a local spin-singlet s -wave pairing on the same orbital³⁴, further enhanced via coherent tunneling of pairs between orbitals (the Suhl-Kondo mechanism)^{62,63}. On the other hand, the multiorbital electronic correlations suppress electron hopping-induced charge fluctuations and effectively bind electrons into intraorbital pairs³³. In this sense, the Coulomb interactions actually help the local pairing, until they are strong enough to drive a transition from the superconductivity to Mott-insulating phase³⁷. Such a local pairing scenario naturally accounts for the dome-shaped dependence of T_c on C_{60} packing density-controlled U ^{31,36,46} as well as the conflicting variation of superconductivity with film thickness in K_3C_{60} and Rb_3C_{60} . In K_3C_{60} , U is relatively small and its enhancement at reduced film thicknesses stabilizes the local pairing and thus enhances superconductivity³⁷, whereas the opposite holds true owing to the already large U in Rb_3C_{60} . A further enhancement of U pushes thin Rb_3C_{60} films closer to a Mott transition and suppresses superconductivity, as observed. In Fig. 5, we show the phase diagram of charged fullerides and discover universal optimal superconductivity at half-filling, no matter how the electronic correlations U change with the alkali metal and film thickness. This finding is unusual and probably stems from a decrease in the dynamical JT-related pair binding energy (U_x , negative) away from half-filling^{61,62}, until the superconductivity vanishes as the U_x changes its sign. For the evenly charged fullerenes, U_2 and U_4 are positive and the JT coupling instead stabilizes two correlated insulating ground states^{61,62}. It is also important to note that an asymmetry of Δ versus x phase diagram relative to half-filling ($x = 3$) occurs as U becomes strong. This is related to a monotone shrinkage of U with the doping x in view of the enhanced Coulomb screening from itinerant electron carriers³⁷. In strongly correlated regimes, a small increase of U below half-filling can

suppress superconductivity significantly and leads to the observed dome asymmetry.

Finally, we note that the large ratio of energy gap Δ to critical temperature (e.g., $2\Delta/k_B T_c > 6.0$) seems to be a generic trait of high- T_c superconductivity in narrow-band systems^{10,20,35,37,49}, including the copper-oxide superconductors⁴⁵. Such a large deviation from the canonical BCS value of 3.53 could be straightforward to understand theoretically in the framework of local nonretarded superconductivity⁵⁸. Experimentally, a similar local pairing mechanism, assisted cooperatively by a dynamic interfacial polaron, has been recently proposed to be responsible for the high- T_c superconductivity in monolayer FeSe epitaxial films grown on SrTiO_3 substrate⁶⁴. A question naturally arises as to whether the local pairing mechanism is applicable to other narrow-band cuprates and multi-band iron pnictides⁶⁵. Another interesting issue is to unravel the nature of pseudogap that ubiquitously emerges from the doped fullerene films with no spatially modulated electronic charge density (Fig. 2a–c). This excludes a possible origin of the pseudogap from charge orders. Whether the pseudogap shares the same mechanism as that of cuprates and how it interplays with high- T_c superconductivity remain unsolved issues that merit further investigations. In any case, our experimental results of fulleride superconductors shed important light on the electron pairing in narrow-band high- T_c superconductors.

Methods

Sample preparations. Our experiments were conducted in a commercial Unisoku 1500 ultra-high vacuum STM facility, connected to an MBE chamber for in situ film preparation. The base pressure of both chambers is lower than 2.0×10^{-10} Torr. C_{60} molecules were evaporated from a standard Knudsen diffusion cell and grew layer-by-layer on nitrogen-doped $\text{Si}(0001)$ wafers ($0.1 \Omega \text{ cm}$) at 473 K, which were pre-graphitized by thermal heating (up to 1600 K) to form bilayer graphene. Desired alkali metal atoms (Rb or Cs) were then deposited from thoroughly outgassed SAES getters on C_{60} films at a low temperature of ~ 200 K step by step, followed by > 3 h of post-annealing at room temperature. The layer index n of Rb_3C_{60} multilayers ($n \leq 3$) is determined from the step height, STM topographies and tunneling dI/dV spectra, which varies significantly with n . The flux rate of C_{60} is therefore calculated by dividing the coverage of fulleride films by growth time, and is used as a reference for the determination of the nominal thickness for thicker fullerenes, e.g., $n = 6$ and 9 in the main text.

Away from half-filling, the electron doping x is calculated directly from the areal density of Rb vacancies (Fig. 3a) or excess Rb dopants (Fig. 3c). For $x \sim 3$, there exist little defect that leads to trivalent fulleride films (Fig. 1a). A single Rb vacancy (excess) is reasonably considered as one missing (additional) Rb dopant relative to Rb_3C_{60} . For higher doping, x is estimated from the coverage of Rb clusters, since the excess Rb dopants are individually undistinguishable. By this method, the estimated x has a statistical error of $< 0.5\%$.

STM measurements. After the sample growth, the fulleride epitaxial films were immediately transferred into our STM chamber for all STM and STS data collections at 4.6 K. A bias voltage was applied to the samples. To accurately characterize the superconductivity and electronic structure of fulleride films, special measures such as grounding and shielding were taken to optimize the stability and spectroscopic resolution of our STM facility. Polycrystalline PtIr tips were used after careful calibration on Ag films grown on Si(111). All STM topographic images were taken in a constant current mode. Tunneling dI/dV spectra and electronic DOS maps were acquired using a standard lock-in technique with modulation frequency $f = 975$ Hz, while the modulation amplitudes were 0.2 meV and 20 meV for measuring the superconducting gaps and wider-energy-range (± 1.0 eV) dI/dV spectra, respectively.

Data availability

All data are available from the corresponding author on reasonable request.

Received: 19 January 2021; Accepted: 30 April 2021;

Published online: 03 June 2021

References

1. Sacpé, B. et al. Localization of preformed Cooper pairs in disordered superconductors. *Nat. Phys.* **7**, 239–244 (2011).

Fig. 5 Unified phase diagram of Δ variation with electronic correlations U and doping. The empty circles and squares distinctively mark the experimental Δ measured in K_3C_{60} and Rb_3C_{60} films, respectively. Contour plots of Δ with a separation of 2 meV are shown in gray dashes. Note that the fulleride superconductivity is always peaked at half-filling at any specific U/W , with W denoting the t_{1u} bandwidth.

2. Mao, Z. Q., Mori, Y. & Maeno, Y. Suppression of superconductivity in Sr_2RuO_4 caused by defects. *Phys. Rev. B* **60**, 610–614 (1999).
3. Song, C. L. et al. Direct observation of nodes and twofold symmetry in FeSe superconductor. *Science* **332**, 1410–1413 (2011).
4. Zhang, G. et al. Bosonic confinement and coherence in disordered Nano diamond arrays. *ACS Nano* **11**, 11746–11754 (2017).
5. Lee, P. A., Nagaosa, N. & Wen, X. G. Doping a Mott insulator: physics of high-temperature superconductivity. *Rev. Mod. Phys.* **78**, 17–85 (2006).
6. Kamihara, Y., Watanabe, T., Hirano, M. & Hosono, H. Iron-based layered superconductor $\text{La}(\text{O}_{1-x}\text{F}_x)\text{FeAs}$ ($x = 0.5 - 0.12$) with $T_c = 26$ K. *J. Am. Chem. Soc.* **130**, 3296–3297 (2008).
7. Liu, B. Nonmagnetic impurity resonance states as a test of superconducting pairing symmetry in CeCoIn_5 . *Phys. Rev. B* **88**, 245127 (2013).
8. Li, J. et al. Local destruction of superconductivity by non-magnetic impurities in mesoscopic iron-based superconductors. *Nat. Commun.* **6**, 7614 (2015).
9. Fan, Q. et al. Plain *s*-wave superconductivity in single-layer FeSe on SrTiO_3 , probed by scanning tunneling microscopy. *Nat. Phys.* **11**, 946–952 (2015).
10. Yamashita, T. et al. Fully gapped superconductivity with no sign change in the prototypical heavy-fermion CeCu_2Si_2 . *Sci. Adv.* **3**, e1601667 (2017).
11. Choi, D. J. et al. Mapping the orbital structure of impurity bound states in a superconductor. *Nat. Commun.* **8**, 15175 (2017).
12. Zhang, G. F. et al. Global and local superconductivity in boron-doped granular diamond. *Adv. Mater.* **26**, 2034–2040 (2014).
13. Zhang, G. F. et al. Yu-Shiba-Rusinov bands in ferromagnetic superconducting diamond. *Sci. Adv.* **6**, eaaz2536 (2020).
14. Keimer, B., Kivelson, S. A., Norman, M. R., Uchida, S. & Zaanen, J. From quantum matter to high-temperature superconductivity in copper oxides. *Nature* **518**, 179–186 (2015).
15. Fernandes, R. M., Chubukov, A. V. & Schmalian, J. What drives nematic order in iron-based superconductors? *Nat. Phys.* **10**, 97–104 (2014).
16. Yazdani, A., Jones, B. A., Lutz, C. P., Crommie, M. F. & Eigler, D. M. Probing the local effects of magnetic impurities on superconductivity. *Science* **275**, 1767–1770 (1977).
17. Balatsky, A. V., Vekhter, I. & Zhu, J. X. Impurity-induced states in conventional and unconventional superconductors. *Rev. Mod. Phys.* **78**, 373–433 (2006).
18. Pan, S. H. et al. Imaging the effects of individual zinc impurity atoms on superconductivity in $\text{Bi}_2\text{Sr}_2\text{CaCu}_2\text{O}_{8+\delta}$. *Nature* **403**, 746–750 (2000).
19. Grothe, S. et al. Bound states of defects in superconducting LiFeAs studied by scanning tunneling spectroscopy. *Phys. Rev. B* **86**, 174503 (2012).
20. Yang, H. et al. In-gap quasiparticle excitations induced by non-magnetic Cu impurities in $\text{Na}(\text{Fe}_{0.96}\text{Co}_{0.03}\text{Cu}_{0.01})\text{As}$ revealed by scanning tunneling spectroscopy. *Nat. Commun.* **4**, 2749 (2013).
21. Petrovic, A. P. et al. A disorder-enhanced quasi-one-dimensional superconductor. *Nat. Commun.* **7**, 12262 (2016).
22. Peng, J. et al. Disorder enhanced superconductivity toward TaS_2 monolayer. *ACS Nano* **12**, 9461–9466 (2018).
23. Zhao, K. et al. Disorder-induced multifractal superconductivity in monolayer niobium dichalcogenides. *Nat. Phys.* **15**, 904–910 (2019).
24. An, C. et al. Long-range ordered amorphous atomic chains as building blocks of a superconducting quasi-one-dimensional crystal. *Adv. Mater.* **32**, 2002352 (2020).
25. Poccia, N. et al. Evolution and control of oxygen order in a cuprate superconductor. *Nat. Mater.* **10**, 733–736 (2011).
26. Heinrich, B. W., Pascual, J. I. & Franke, K. J. Single magnetic adsorbates on *s*-wave superconductors. *Prog. Surf. Sci.* **93**, 1–19 (2018).
27. David, W., Ibberson, R. M., Dennis, T. J. S., Hare, J. P. & Prassides, K. Structural phase-transition in the fullerene C_{60} . *Europhys. Lett.* **18**, 219–225 (1992).
28. Stephens, P. W. et al. Structure of single-phase superconducting K_3C_{60} . *Nature* **351**, 632–634 (1991).
29. Hiroshima, I. et al. Orientational disordering of C_{60} in $\text{Na}_2\text{RbC}_{60}$ superconductor. *Solid State Commun.* **87**, 945–949 (1993).
30. Prassides, K. et al. Crystal structure, bonding, and phase transition of the superconducting $\text{Na}_2\text{CsC}_{60}$ fulleride. *Science* **263**, 950–954 (1994).
31. Takabayashi, Y. et al. The disorder-free non-BCS superconductor Cs_3C_{60} emerges from an antiferromagnetic insulator parent state. *Science* **323**, 1585–1590 (2009).
32. Potočnik, A. et al. Jahn-Teller orbital glass state in the expanded fcc Cs_3C_{60} fulleride. *Chem. Sci.* **5**, 3008–3017 (2014).
33. Han, J. E., Gunnarsson, O. & Crespi, V. H. Strong superconductivity with local Jahn-Teller phonons in C_{60} solids. *Phys. Rev. Lett.* **90**, 167006 (2003).
34. Nomura, Y., Sakai, S., Capone, M. & Arita, R. Unified understanding of superconductivity and Mott transition in alkali-doped fullerenes from first principles. *Sci. Adv.* **1**, e1500568 (2015).
35. Koller, D. et al. Energy gap in superconducting fullerenes: optical and tunneling studies. *Phys. Rev. Lett.* **77**, 4082–4085 (1996).
36. Capone, M., Fabrizio, M., Castellani, C. & Tosatti, E. Colloquium: Modeling the unconventional superconducting properties of expanded A_3C_{60} fullerenes. *Rev. Mod. Phys.* **81**, 943–958 (2009).
37. Ren, M. Q. et al. Direct observation of full-gap superconductivity and pseudogap in two-dimensional fullerenes. *Phys. Rev. Lett.* **124**, 187001 (2020).
38. Han, S. et al. Visualizing molecular orientational ordering and electronic structure in Cs_3C_{60} fulleride films. *Phys. Rev. B* **101**, 085413 (2020).
39. Kämmerer, S., Kob, W. & Schilling, R. Dynamics of the rotational degrees of freedom in a supercooled liquid of diatomic molecules. *Phys. Rev. E* **56**, 5450–5461 (1997).
40. Yildirim, T., Hong, S., Harris, A. B. & Mele, E. J. Orientational phases for M_3C_{60} . *Phys. Rev. B* **48**, 12262–12277 (1993).
41. Gelfand, M. P. & Lu, J. P. Orientational disorder and electronic states in C_{60} and A_3C_{60} where A is an alkali metal. *Phys. Rev. Lett.* **68**, 1050–1053 (1992).
42. Normura, Y., Nakamura, K. & Arita, R. Ab initio derivation of electronic low-energy models for C_{60} and aromatic compounds. *Phys. Rev. B* **85**, 155452 (2012).
43. Ceulemans, A., Chibotaru, L. F. & Cimpoesu, F. Intramolecular charge disproportionation and the band structure of A_3C_{60} superconductors. *Phys. Rev. Lett.* **78**, 3725–3728 (1997).
44. Suzuki, S. & Nakao, K. Electron-electron and electron-phonon interactions in alkali-metal-doped C_{60} . *Phys. Rev. B* **52**, 14206–14218 (1995).
45. Fischer, Ö., Kugler, M., Maggio-Aprile, I., Berthod, C. & Renner, C. Scanning tunneling spectroscopy of high-temperature superconductors. *Rev. Mod. Phys.* **79**, 353–419 (2007).
46. Gasuhiro, A. Y. et al. Polymorphism control of superconductivity and magnetism in Cs_3C_{60} close to the Mott transition. *Nature* **466**, 221–225 (2010).
47. Satoshi, K. & Yukio, T. Tunneling effects on surface bound states in unconventional superconductors. *Rep. Prog. Phys.* **63**, 1641–1724 (2000).
48. Yeh, N. C. et al. Evidence of doing-dependent pairing symmetry in cuprate superconductors. *Phys. Rev. Lett.* **87**, 087003 (2001).
49. Liu, X. et al. Evidence of nematic order and nodal superconducting gap along [110] direction in RbFe_2As_2 . *Nat. Commun.* **10**, 1039 (2019).
50. Luh, Y. Bound state in superconductors with paramagnetic impurities. *Acta Phys. Sin.* **21**, 75 (1965).
51. Shiba, H. Classical spins in superconductors. *Prog. Theor. Phys.* **40**, 435–451 (1968).
52. Rusinov, A. I. On the theory of gapless superconductivity in alloys containing paramagnetic impurities. *Sov. JETP* **29**, 1101 (1969).
53. Yang, X. et al. Observation of short-range Yu-Shiba-Rusinov states with threefold symmetry in layered superconductor $2\text{H}-\text{NbSe}_2$. *Nanoscale* **12**, 8174–8179 (2020).
54. Farinacci, L. et al. Tuning the coupling of an individual magnetic impurity to a superconductor: quantum phase transition and transport. *Phys. Rev. Lett.* **121**, 196803 (2018).
55. Migdal, A. B. et al. Interaction between electrons and lattice vibrations in a normal metal. *Sov. Phys. JEPT* **34**, 996–1001 (1958).
56. Pietronero, L., Strässler, S. & Grimaldi, C. Nonadiabatic superconductivity. I. Vertex correlations for the electron-phonon interactions. *Phys. Rev. B* **52**, 10516–10529 (1995).
57. Grimaldi, C., Pietronero, L. & Strässler, S. Nonadiabatic superconductivity. II. Generalized Eliashberg equation beyond Migdal's theorem. *Phys. Rev. B* **52**, 10530–10546 (1995).
58. Micnas, R., Ranninger, J. & Robaszkiewicz, S. Superconductivity in narrow-band systems with local nonretarded attractive interactions. *Rev. Mod. Phys.* **62**, 113–171 (1990).
59. Grigorishin, K. V. The role of electron-vibron interaction and local pairing in conductivity and superconductivity of alkali-doped fullerenes. *Phys. C* **562**, 56–69 (2019).
60. Auerbach, A., Manini, N. & Tosatti, E. Electron-vibron interactions in charged fullerenes. I. Berry phases. *Phys. Rev. B* **49**, 12998–13007 (1994).
61. Manini, N., Tosatti, E. & Auerbach, A. Electron-vibron interactions in charged fullerenes. II. Pair energies and spectra. *Phys. Rev. B* **49**, 13008–13016 (1994).
62. Suhl, H., Matthias, B. T. & Walker, L. R. Bardeen-Cooper-Schrieffer theory of superconductivity in the case of overlapping bands. *Phys. Rev. Lett.* **3**, 552–554 (1959).
63. Kondo, J. Superconductivity in transition metals. *Prog. Theor. Phys.* **29**, 1–9 (1963).
64. Zhang, S. Y. et al. Enhanced superconducting state in FeSe/SrTiO_3 by a dynamic interfacial polaron mechanism. *Phys. Rev. Lett.* **122**, 066802 (2019).
65. Keller, H., Bussmann-Holder, A. & Müller, K. A. Jahn-Teller physics and high- T_c superconductivity. *Mater. Today* **11**, 38–46 (2008).

Acknowledgements

We thank H.Y. and H.W.L. for fruitful discussions. The work was financially supported by the Natural Science Foundation of China (grants no. 51788104, no. 11634007, and no. 11774192), the Ministry of Science and Technology of China (2017YFA0304600, 2016YFA0301004, 2018YFA0305603), and in part by the Beijing Advanced Innovation Center for Future Chip.

Author contributions

C.L.S., X.C.M., and Q.K.X. conceived and designed the experiments. S.Z.W., S.H., and M.Q.R. carried out the MBE growth and STM measurements. M.Q.R., S.Z.W., F.J.C., and C.L.S. analyzed the data and wrote the manuscript with comments from all authors.

Competing interests

The authors declare no competing interests.

Additional information

Supplementary information The online version contains supplementary material available at <https://doi.org/10.1038/s42005-021-00619-y>.

Correspondence and requests for materials should be addressed to C.-L.S.

Reprints and permission information is available at <http://www.nature.com/reprints>

Publisher's note Springer Nature remains neutral with regard to jurisdictional claims in published maps and institutional affiliations.



Open Access This article is licensed under a Creative Commons Attribution 4.0 International License, which permits use, sharing, adaptation, distribution and reproduction in any medium or format, as long as you give appropriate credit to the original author(s) and the source, provide a link to the Creative Commons license, and indicate if changes were made. The images or other third party material in this article are included in the article's Creative Commons license, unless indicated otherwise in a credit line to the material. If material is not included in the article's Creative Commons license and your intended use is not permitted by statutory regulation or exceeds the permitted use, you will need to obtain permission directly from the copyright holder. To view a copy of this license, visit <http://creativecommons.org/licenses/by/4.0/>.

© The Author(s) 2021